

Super-resolving Real-world Image Illumination Enhancement: A New Dataset and A Conditional Diffusion Model

Yang Liu^{1,*}, Yaofang Liu^{2,*}, Jinshan Pan³, Yuxiang Hui¹, Fan Jia¹, Raymond H. Chan⁴, Tieyong Zeng¹

¹ The Chinese University of Hong Kong, ² City University of Hong Kong

³ Nanjing University of Science and Technology, ⁴ Lingnan University

Abstract

Most existing super-resolution methods and datasets have been developed to improve the image quality in well-lighted conditions. However, these methods do not work well in real-world low-light conditions as the images captured in such conditions lose most important information and contain significant unknown noises. To solve this problem, we propose a SRRIE dataset with an efficient conditional diffusion probabilistic models-based method. The proposed dataset contains 4800 paired low-high quality images. To ensure that the dataset are able to model the real-world image degradation in low-illumination environments, we capture images using an ILDC camera and an optical zoom lens with exposure levels ranging from -6 EV to 0 EV and ISO levels ranging from 50 to 12800. We comprehensively evaluate with various reconstruction and perceptual metrics and demonstrate the practicabilities of the SRRIE dataset for deep learning-based methods. We show that most existing methods are less effective in preserving the structures and sharpness of restored images from complicated noises. To overcome this problem, we revise the condition for Raw sensor data and propose a novel time-melding condition for diffusion probabilistic model. Comprehensive quantitative and qualitative experimental results on the real-world benchmark datasets demonstrate the feasibility and effectiveness of the proposed conditional diffusion probabilistic model on Raw sensor data. Code and dataset will be available at <https://github.com/Yaofang-Liu/Super-Resolving>.

1. Introduction

Super-resolving real-world illumination enhancement images captured in dark scenes has recently attracted increasing attention due to its potential applications in practical computational imaging, such as traffic detection and night photography. The objective of this task is to restore rich structural details and enhance unbiased colors as much as possible from the degraded images. A real-world im-

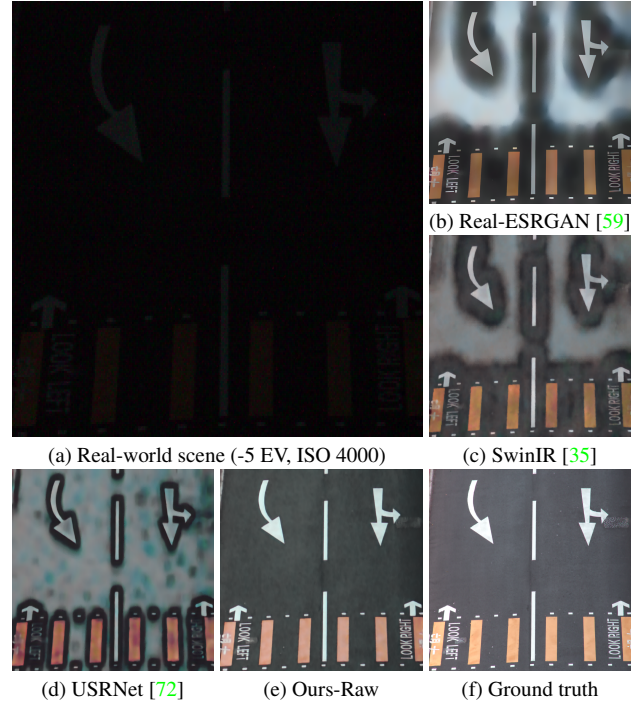


Figure 1. Visual comparisons ($\times 4$ SR) on the SRRIE dataset for super-resolving real-world image illumination enhancement tasks. The low-quality image is captured with the camera settings of -5 EV and ISO 4000. The complicated noises make it difficult to restore truthful image information. Our conditional DPM-based method using Raw sensor data generates better structural details.

age captured with camera settings of ISO 4000 and -5 EV is shown in Figure 1 (a). In real-world low-light photography, it is necessary to increase the ISO level to capture with a safe shutter speed to avoid obtaining blurry images. However, high ISO levels will introduce severe noise in images. These real-world degradation processes make the joint image illumination enhancement and super-resolution problems highly ill-posed.

To restore images suffering from joint degradation problems, we could employ existing single image illumination enhancement methods [37, 62, 69, 32] and single im-

*Equal Contribution.

age super-resolution methods [72, 59, 35, 69] separately in a cascaded manner. However, the intermediate output will suffer from significant information loss, e.g., the over-smoothing effects [30] if we use a CNN for the first stage. Moreover, the accumulation errors from the first stage will be further amplified in the second stage. To address these problems, another approach is to directly fine-tune a super-resolution network [72, 59, 35, 69] to learn high-resolution images from low-light images in an end-to-end manner on the low-light datasets. However, widely used low-light datasets [63, 9, 7] does not contain real-world normal-light high-resolution images as the ground truth. While the widely used super-resolution datasets [43, 70, 6, 3, 8, 10, 74, 64] does not contain real-world degraded low-light images. To solve this problem, the RELISUR [1] datasets have been proposed using a DSLR cameras to capture paired sRGB data. However, the RELISUR dataset neglects the noise model and is captured with low ISO levels from 100 to 400. We note that the low ISO levels and less noises simplify the real-world degradation model and will ease the learning process from low-quality to high-quality images.

To address these problems, we introduce a novel image dataset called SRRRIE for super-resolving real-world image illumination enhancement tasks. The SRRRIE dataset poses a challenging task for image super-resolution due to the low light caused by a wide range of under-exposure levels from -6 EV to 0 EV, and real-world noises caused by large ISO levels from 50 to 12800. Due to the severe degradation in real-world imaging, existing methods performs less effectively to restore images that lose most important information and contain significant unknown noises. We then propose a new conditional diffusion model that progressively generates truthful structural details from severely degraded Raw images. We demonstrate that Raw sensor data contains more lossless information than sRGB images, and we revise the condition for Raw sensor data to adapted to DPM. To improve the consistency and robustness of the reverse generation process and boost the restoration and enhancement results, we propose a novel time-melding condition by fusing temporal coherence information across relevant time points. We conduct comprehensive benchmark experiments on our SRRRIE dataset. The results show that our proposed method (Figure 1 (e)) achieves promising results against existing methods (Figures 1 (b)-(d)).

The main contributions of this work are as follows:

- We have analyzed the real-world noises introduced by high ISO levels in real-world imaging and propose a large-scale SRRRIE dataset. This dataset comprises paired low-high quality image sequences and aims to facilitate the super-resolution of real-world illumination enhancement from Raw sensor data.
- We revise the condition for Raw sensor data to adapt to conditional DPM, thus lossless image structural de-

tails can be extracted. We further propose a novel time-melding condition implemented by fusing time-consistency information across relevant time points to effectively improve the reverse generation process.

- We present a new conditional diffusion model with the proposed two effective conditions for Raw sensor data, which progressively generates sharp image structural details from complex noises. Through both quantitative and qualitative assessments on our real-world SRRRIE datasets, we demonstrate the feasibility and effectiveness of our proposed dataset and method.

2. Related Work

We recently have witnessed significant advances in real-world benchmark datasets and methods for single image illumination enhancement and/or super-resolution tasks. A comprehensive review is beyond the scope of this work. We present the most related ones briefly within proper contexts.

Image illumination enhancement datasets and methods.

Several unpaired low-light image datasets [31, 42, 20] without ground truth normal-light images are used by traditional methods [55, 31, 13, 24, 20, 34, 45]. However, these histogram-based and variational-based methods cannot be adequate to images with various lighting conditions. Wei et al. propose the paired LOL dataset [63]. SID [9] introduces a Raw dataset containing short-long exposure night-time images. The SICE dataset [7] contains multi-exposed image sequences and the reference images are synthesized by using the exposure fusion methods. Based on these large-scale datasets, EnlightenGAN [26] performs restoration via a generative network. Zero-DCE [32] iteratively enhances a given input image by estimating a set of best-fitting light-enhancement curves in an unsupervised manner. However, these unsupervised learning methods encounter artifacts and color distortion problems. Most recent methods [63, 37, 76, 68, 62] could achieve favorable results w.r.t. reconstruction metrics, but they are less effective on real Raw low-light images with other degradation processes such as real-world noises or low resolution.

Image super-resolution datasets and methods.

The widely used datasets [43, 70, 6, 3] facilitate the training of deep image super-resolution methods. Seminal ResNet-based methods [28, 56, 36, 75, 72] using these datasets and demonstrate the effectiveness against traditional non-deep learning methods [66, 57]. However, these pioneered works assume that the SR kernels in the degradation process are known and are fixed to the bicubic one, where the low-resolution images are downsample from the HR one with bicubic interpolation. To overcome the over-smoothing problem, GAN-based methods [30, 61, 60, 71] present considerable potentials in generating rich details. However, unpleasant artifacts and untruthful structures are usually introduced. In [41], normalizing flow is proposed to generate the distributions of realistic structural details for high-

resolution images. Transformer-based methods [11, 35, 19] achieve remarkable performance using the attention mechanism. To fix the domain gap between synthetic datasets and real-world datasets, both low-resolution and high-resolution images are captured with DSLR and smartphone cameras in recently proposed datasets including RealSR [8], City100 [10], SR-RAW [74], and DRealSR [64] datasets. The most related dataset to ours is the RELLISUR [1] dataset. However, these datasets are captured in well-lighted condition with low ISO levels, e.g., 100-400. They neglect the noise model and rarely explore how real-world noises affect the design of deep image super-resolution solvers.

Diffusion probabilistic models for image restoration. Diffusion probabilistic models [23, 51, 53, 54, 16] forming a novel family of deep generative models [67] have showed state-of-the-art performance in image restoration [27, 12, 46, 49]. These pioneered works reveal that the diffusion models have strong capability in generating high-fidelity and perceptually pleasing structures and details [14]. Existing methods [23, 27] commonly adopt the Gaussian noises for the diffusion process. Cold diffusion [5] replaces the Gaussian noises with various degradation models and shows remarkable restoration results across multiple tasks. Conditional diffusion models achieves noticeable results in face image super-resolution [33, 49, 46]. Whang et al. [65] train a stochastic sampler for blind deblurring based on conditional diffusion models. PatchDM [44] is proposed to restore hazy and rainy images. However, these methods rarely explore how real-world noises affect the design and performance of diffusion probabilistic models and how to accommodate to the real Raw sensor data.

Different from existing datasets and methods, our collected SRRRIE dataset captures real Raw sensor data (Section 3). The low-resolution images suffer from complicated real-world noises. To solve this problem, we propose an effective conditional DPM-based method with two novel conditions (Section 5) to progressively generate photo-realistic structural details from lossless Raw images.

3. SRRRIE Dataset

To model the real-world degradation process for Super-resolving image illumination enhancement tasks, we collect the real-world SRRRIE dataset that contains paired low-light images (Raw/sRGB) and high-resolution images (sRGB) to enables the learning process for deep neural networks. Our data pipeline explores the complicated real-world degradation processes including real-world noises, low light and low resolution, which differentiate our data and method framework from existing data and methods.

3.1. Data collection and processing pipeline

We use a Sony A7 IV camera equipped with a Tamron 28-200mm zoom lens to collect 400 paired image sequences from 400 different scenes for super-resolving real-

world illumination enhancement tasks. Figure 2 illustrates the main collection and processing steps of our proposed SRRRIE dataset for one scene, where the Raw sensor data is collected to better preserve the real-world degradation process. We employ the camera ISP to convert Raw sensor data to corresponding sRGB images and retain the centered croppings. Each image sequence contains paired low-light images suffering from real-world noises under varying ISO levels, and the corresponding noise-free normal-light high-resolution images. We illustrate the details as follows.

Low-light image sequences. We capture 9 Raw images for each low-light image sequence using the auto bracketing exposure mode of the camera in an under-exposure manner ranging from -6 EV to -2 EV. The only variable camera parameter to achieve the real-world low-light sequences for each scene is the exposure time and the others are fixed. We use a fixed ISO level for each scene, while the ISO level varies from 800 to 12800 according to different scene conditions. We note that the camera ISO parameter is one of the key settings in real-world low-light imaging to capture properly exposed image in poor lighting conditions. It is usually necessary to increase the ISO level to ensure the safe shutter speed otherwise we will capture a blurry image. However, as higher ISO levels will inevitably degrade the image quality, the image structures and details are corrupted by complicated noises. We note that a wide range of ISO levels with complicated real-world noises for super-resolving real-world illumination enhancement on real sensor data makes the restoration problems high ill-posed, which differentiates our data pipeline from existing datasets [63, 9, 74, 1].

High-resolution image sequences. The high-resolution image sequences are achieved by 1x, 2x and 4x optical zoom using 0 EV as the size of an imaging object is approximately linear to the focal length of the camera.. For example, we use a focal length of 30 mm, 60 mm, and 120 mm for indoor scenes, and a focal length of 50 mm, 100 mm, and 200 mm for outdoor scenes, which respectively correspond to $\times 1$, $\times 2$, and $\times 4$ image super-resolution tasks. We capture 10 successive Raw images $\{I_n^m\}_{n=1}^{10}$ for each optical zoom level using a continuous capture mode of the camera and robustly estimate the mean image to obtain the high-quality noise-free ground truth images $\{J_m\}_{m=1}^3$:

$$J_m = \Psi_{mean}(g_{crop}(f_{ISP}(\{I_n^m\}_{n=1}^{10}))), \quad m = 1, 2, 3, \quad (1)$$

where m denotes three optical zoom levels. f_{ISP} , g_{crop} and Ψ_{mean} is the camera ISP, center crop operator and robust mean image estimation method [2], respectively. We then perform intensity and spatial alignment to obtain the rectified ground truth images $\{\bar{J}_m\}_{m=1}^3$:

$$\bar{J}_m = \Phi_{align}(J_m - \mu_m + \mu_1), \quad m = 1, 2, 3, \quad (2)$$

where $\{\mu_m\}_{m=1}^3$ are corresponding mean intensities of $\{J_m\}_{m=1}^3$. Φ_{align} is a spatial alignment function based on

Super-resolving Real-world Image Illumination Enhancement Dataset (SRRRIE)

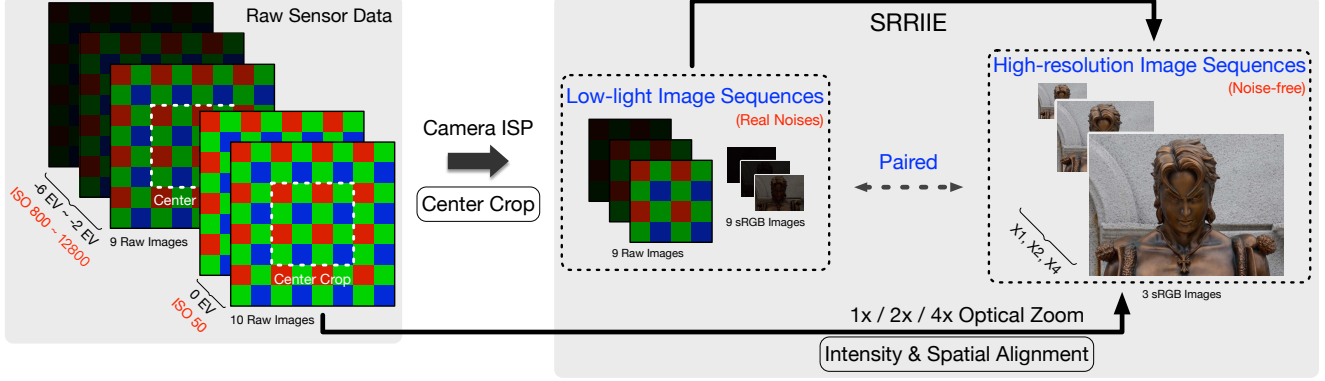


Figure 2. Our data collection and processing pipeline for one scene. An ILDC with an optical zoom lens is used to collect real Raw sensor data with a wide range of EV and ISO levels. Camera ISP is employed to convert Raw images to sRGB images and only the centered croppings are retained. Each low-light image sequence contain 9 low-light Raw/sRGB images with complicated real-world noises and low intensities. While each high-resolution image sequence contains 3 noise-free normal-light high-resolution images as the ground truth. These paired images model the real-world degradation process for super-resolving image illumination enhancement (SRRRIE) tasks.

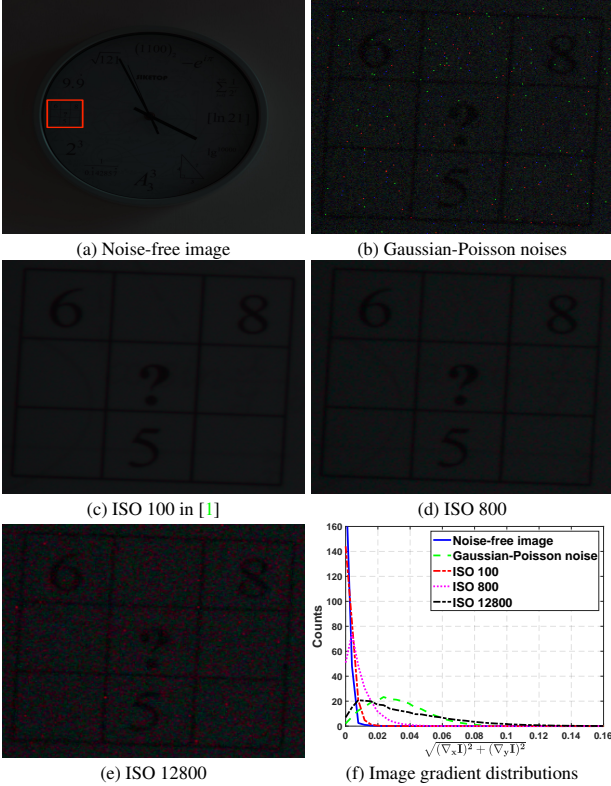


Figure 3. Simple cases to illustrate the motivation. (b)-(e) are the corresponding cropped and zoomed-in regions as denoted by the red box in (a). The synthetic Gaussian-Poisson noisy image (b) or the image captured with the low ISO level (c) deviates largely from real-world noisy images (d) - (e) in terms of visual comparison and statistical image gradient distributions (f).

SIFT descriptors [40] to deal with the distortions caused by optical zoom. The only variable camera parameter to achieve the real-world high-resolution sequences for each scene is the focal length, and the others are fixed.

In total, we capture 400 image sequences which contain

Table 1. Image quality assessment for different image degradation processes in our SRRRIE dataset.

Degradation Process		PSNR \uparrow	SSIM \uparrow	LPIPS \downarrow
Exposure	-2.0 EV	10.74	0.5241	0.7543
	-4.0 EV	9.20	0.3612	0.9568
	-6.0 EV	8.72	0.3011	1.0095

4800 images for 100 indoor scenes and 300 outdoor scenes. Each image sequence contains 12 images, i.e., 9 low-light images (Raw/sRGB) and 3 high-resolution images (sRGB). These images are paired to model the real-world degradation process for Super-resolving image illumination enhancement tasks. We selectively split 400 image sequences into 300 and 100 sets for training and test, respectively.

During the data collection process for each scene, we use fixed camera parameters to maximize imaging authenticity, e.g., aperture, white balance, etc. We use the aperture size ranging from f/8 to f/19 to balance the image quality and depth of field considering the depth of objects. We mount the camera on a sturdy tripod and use a remote shooting manner. The camera stabilization and noise reduction functions of the camera are turned off. We capture the images by manual focus and central partial metering. The collected images that suffer from undesired defects including external illumination changes, blurs and unaligned objects have been manually discarded. We also avoid other ethical issues.

3.2. Degradation analysis on the dataset

To analyze the challenge of the highly ill-posed real-world degradation process, we show an indoor example captured with 0 EV in Figure 3. We crop and zoom-in the corresponding regions denoted by the red box in Figure 3 (a) for Figures 3 (b)-(e). The noise-free image (Figure 3 (a)) is achieved by robustly averaging 10 images [2] captured with ISO 50. The synthetic Gaussian-Poisson noises are widely used to add to the noise-free image in exist-

ing methods. However, the synthetic noises deviate significantly from real noises as shown in Figure 3 (b) ($\sigma_G = 0.04, \lambda_P = 0.001$). Several benchmark datasets such as the RELLISUR [1] dataset use low ISO levels (Figure 3 (c)), but we note that it will easily cause significant blurs without using a tripod due to long exposure time. On the contrary, Figures 3 (b)-(e) show the real-world noises captured using ISO 800 and 12800 to guarantee the safe shutter speed. As the ISO level increases, the heavier real noises severe degrade the image quality and make this problem highly ill-posed. Figure 3 (f) further demonstrates that the low-light images differ widely in image gradient distribution. Table 1 summarizes the severe information loss compared to the ground truth in terms of PSNR, SSIM and LPIPS metrics due to the superposition of a wide range of under-exposure levels and high ISO levels used in our dataset. The severely degraded image quality makes the inverse problems much more difficult to learn with existing deep solvers.

4. Revisiting DPM

Although we could apply existing methods directly to our SRRRIE dataset, there are still significant challenges due to the highly ill-posed nature of the problem. To address these issues and restore high-quality images from degraded low-quality counterparts, we propose a conditional diffusion model-based method. To aid the subsequent presentation of our method, we briefly review the diffusion probabilistic models (DPM).

DPM [51, 23] are generative models that learn a Markov Chain to gradually transform a Gaussian noise distribution into the target data distribution. To accelerate the sampling speed, DDIM [52] introduces a generalized non-Markovian diffusion process which involves the following inference distributions indexed by a real vector $\sigma \in \mathbb{R}_{\geq 0}^T$:

$$q_\sigma(x_{1:T} | x_0) := q_\sigma(x_T | x_0) \prod_{t=2}^T q_\sigma(x_{t-1} | x_t, x_0), \quad (3)$$

where the marginals $q_\sigma(x_T | x_0)$ and $q_\sigma(x_{t-1} | x_t, x_0)$ are Gaussian distributions $\mathcal{N}(x_T; \sqrt{\alpha_T}x_0, (1 - \sqrt{\alpha_T})\mathbf{I})$ and $\mathcal{N}(x_{t-1}; \mu_t(x_t, x_0), \sigma_t^2\mathbf{I})$, respectively. $\alpha_{1:T} \in (0, T]^T$ is a decreasing sequence which could be manually configured or learned jointly [23]. Starting from a standard normal prior $p(x_T) = \mathcal{N}(x_T; \mathbf{0}, \mathbf{I})$, the reverse process involves the following Markov Chain:

$$p_\theta(x_{0:T}) := p(x_T) \prod_{t=1}^T p_\theta^{(t)}(x_{t-1} | x_t), \quad (4)$$

that employs learned Gaussian denoisers $\mu_\theta(x_t, t)$ to predict $\mu_t(x_t, x_0)$. The denoisers are trained to perform noise reduction while progressively preserve relevant signal information to restore cleaner images. To train the denoisers, the variational inference objective [23, 16, 52] is employed to optimize θ which can be simplified to:

$$L_\theta^{(t-1)} = \mathbb{E}_{x_0, \epsilon_t, t} [\|\epsilon_t - \epsilon_\theta(\sqrt{\alpha_t}x_0 + \sqrt{1 - \alpha_t}\epsilon_t, t)\|^2], \quad (5)$$

The alternative reparameterization of μ_θ is used by ϵ_θ with a re-weighted optimization strategy [23, 52]. Formally, the one-step generation process of DDIM from x_t to x_{t-1} using the trained denoisers is performed by:

$$x_{t-1} = \sqrt{\alpha_{t-1}}\hat{\mu}_\theta(x_t, t) + \hat{r}_\theta(x_t, t) + \sigma_t\epsilon_t, \quad (6)$$

where $\hat{\mu}_\theta(x_t, t) = (x_t - \sqrt{1 - \alpha_t} \cdot \epsilon_\theta(x_t, t))/\sqrt{\alpha_t}$ is the predicted x_0 , while $\hat{r}_\theta(x_t, t) = \sqrt{1 - \alpha_{t-1} - \sigma_t^2} \cdot \epsilon_\theta(x_t, t)$ is a residual term directed to x_t . We set $\sigma_t = 0$ to achieve the deterministic implicit sampling.

Conditional diffusion models [16, 46, 48, 44] aim to generate samples of x that closely match the data distribution conditioned on \tilde{x} , without modifying the underlying diffusion process $q_\sigma(x_{1:T} | x_0)$. The condition \tilde{x} is usually injected into Eqs. (4) and (13) and the correspond revised Eq. (6) is:

$$x_{t-1} = \sqrt{\alpha_{t-1}}\hat{\mu}_\theta(x_t, \tilde{x}, t) + \hat{r}_\theta(x_t, \tilde{x}, t) + \sigma_t\epsilon_t, \quad (7)$$

where x_t and \tilde{x} can be concated [44] or linearly added [48].

5. Conditional DPM-Based Method

Based on above analysis, we propose the conditional DPM-based method with two novel conditions. Figure 4 shows an overview of our approach.

5.1. Revised condition for Raw sensor data

The low-light image sequences of our SRRRIE dataset contains both Raw and sRGB images. To bridge the domain gap, we employ an end-to-end U-Net [47] similar to [9] to learn a mapping from Raw images to sRGB images. We modify the last convolutional layer with a integrated gamma correction function to adjust the brightness and contrast of learned deep features. The reverse process defined in Eqs. (4) and (13) can then be revised with the condition $\pi(\tilde{x})$. Correspondingly, we update Eq. (7) use the revised $\epsilon_\theta(x_t, \pi(\tilde{x}), t)$:

$$x_{t-1} = \sqrt{\alpha_{t-1}}\hat{\mu}_\theta(x_t, \pi(\tilde{x}), t) + \hat{r}_\theta(x_t, \pi(\tilde{x}), t) + \sigma_t\epsilon_t, \quad (8)$$

where π represents an identity mapping if \tilde{x} is a sRGB image otherwise π denotes the learnable U-Net. x_t and $\pi(\tilde{x})$ are concatenated in a channel-wise manner.

5.2. Time-melding condition

We note that the involved Markov Chain in the reverse process defined in Eq. (4) contains progressively generated $x_{0:T}$ from sequenced time points $\{1, \dots, t, \dots, T\}$. The intermediate individuals x_{t-1} could be obtained from x_t via a one-step process defined in Eq. (8) using the learned denoisers. However, we observe that there exists uncertainties in its estimations $x_{0:T}$ of the underlying probability distributions $p_\theta^{(t)}(x_{t-1} | x_t, \pi(\tilde{x}))$. For example, the generated intermediate sequences x_{t-1}, x_t, x_{t+1} may contain inconsistent structural details. Therefore we propose to define the following time-melding condition:

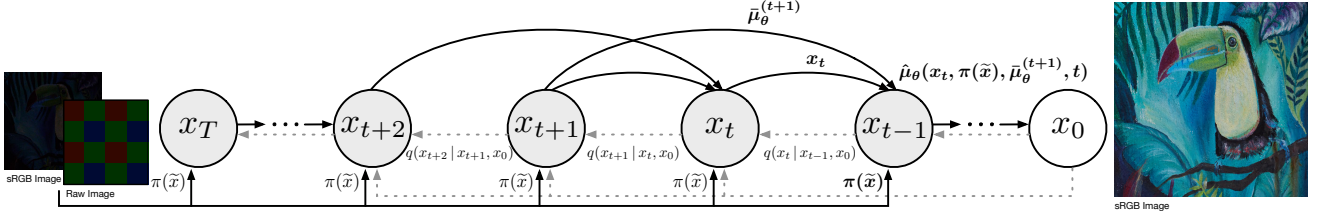


Figure 4. An overview of our conditional DPM with the forward diffusion (dashed line) and reverse process (solid line). Our method generates photo-realistic image structural details conditioned on Raw sensor data $\pi(\tilde{x})$ (Eq. (9)). The proposed time-melding condition (Eq. (9)) improves the reverse generation process (Eq. (10)) by capturing temporal coherence and consistency across relevant time points.

$$\bar{\mu}_\theta^{(t)} = \hat{\mu}_\theta(x_t, \pi(\tilde{x}), \bar{\mu}_\theta^{(t+1)}, t), \quad (9)$$

where we implement this temporal fusion for x_t , $\pi(\tilde{x})$ and $\bar{\mu}_\theta^{(t+1)}$ by a channel-wise concatenated operator such that the conditions will re-weighted adaptively by the denoiser $\hat{\mu}_\theta(\cdot, t)$. We then use to time-melding condition to revise Eq. (8) and x_{t-1} can be predicted as:

$$x_{t-1} = \sqrt{\alpha_{t-1}} \hat{\mu}_\theta(x_t, \pi(\tilde{x}), \bar{\mu}_\theta^{(t+1)}, t) + \hat{r}_\theta(x_t, \pi(\tilde{x}), \bar{\mu}_\theta^{(t+1)}, t) + \sigma_t \epsilon_t, \quad (10)$$

The time-melding conditions $\{\bar{\mu}_\theta^{(t)}\}_{t=1}^T$ are concatenated recursively according to Eq. (9). We set $\bar{\mu}_\theta^{(T)} = x_0$. The goal of the time-melding condition is to capture the temporal coherence across wide yet relevant time points as a single image x_t may not provide enough information. This technique takes advantage of the observation that the information lost in one time point may be available in another time point, thus facilitates preserving as much detail and visual fidelity as possible for the progressively generation process. By fusing valuable information from different time points, the ill-conditioning issues of the real-world degradation process are mitigated, which improves the consistency and robustness of the reverse generation process.

6. Experimental Results

We evaluate our method against state-of-the-art illumination enhancement methods and super-resolution methods on our SRRRIE dataset. We perform comprehensive experiments, and only show parts of representative results in the main paper. Please visit our supplemental material for more extensive results. We will release our SRRRIE dataset, source codes, and trained diffusion models to the public.

6.1. Implementation details

We employ a U-Net like in [52, 5] as the denoiser in our solution, which has 7 residual blocks, and the number of filters are set to 64, 128, 256, 512, respectively. In the learning process, we use the ADAM optimizer [29] with parameters $\beta_1 = 0.9$, $\beta_2 = 0.999$, and $\epsilon = 10^{-8}$. The batch size is set to be 4. The learning rate is initialized as 2×10^{-4} which is updated by SGDR [39]. The parameters are initialized randomly. We set $T = 50$ for the DPM. During training, the input Raw images and ground truth sRGB images are randomly cropped in a paired manner. We pack

each 2×2 block in the Raw Bayer mosaic image into 4 channels denoting for the RGGB image. We randomly crop non-overlapping 50,000 256×256 (512×512 and 1024×1024 for $\times 2$ and $\times 4$ HR) paired patches for training. The entire network is trained using the PyTorch framework. 900 and 900 full-resolution images are used for the validation and test phase, where each high-resolution ground truth image corresponds to 9 low-light low-resolution input images.

6.2. Comparisons with the state-of-the-arts

Evaluation Metrics. Our proposed SRRRIE dataset contains 4800 paired low-high quality images. We employ PSNR and SSIM on the Y channel in the YCbCr color space to evaluate the reconstruction accuracy. We employ LPIPS [73], DISTS [17] and FID [50] in sRGB color space to evaluate the human perception of image quality, which have been validated effectively especially in generation tasks of image structures and details. Higher PSNR and SSIM values indicate higher reconstruction quality, while lower LPIPS, DISTS, and FID values indicate higher perceptual quality. All the methods are strictly evaluated with the same settings on the 900 full-resolution test images.

Quantitative and qualitative results. Table 2 shows the quantitative evaluations on different benchmark datasets, where the results of the state-of-the-art methods are obtained using the corresponding publicly available codes and models for fair comparisons. The proposed method achieves favorable restored images compared to state-of-the-art methods in terms of reconstruction and perceptual metrics. All of the compared methods are strictly evaluated with the same settings. We fine-tune the SOTA methods using their officially released pre-trained models to achieve better results instead of training from scratch. Figure 5 shows a challenging portrait image captured with the under-exposure level of -3 EV and ISO 3200. The complicated noises and low light discourage existing methods as the assumed degradation models deviate from those in this real-world low-light noisy case. The ResNet-based methods [72] suffer from over-smoothing problems. GAN-based methods [59] generate unpleasant artifacts and untruthful colors. Attention-based methods [69, 35] perform less effectively in this real-world low-contrast noisy case. In contrast, our method generate perceptually pleasing results and preserve more structural details.

Table 2. Quantitative evaluations for the state-of-the-art methods on our SRRRIE dataset in terms of PSNR, SSIM, LPIPS [73], DISTS [17] and FID [50] metrics. We fine-tune the SOTA methods using officially released pre-trained models until they converge. Our method achieves favorable results w.r.t. reconstruction and perceptual metrics against the state-of-the-art methods for Super-resolving real-world illumination enhancement. The green and blue color denotes the best and second-best performance of the evaluated methods, respectively.

Method	$\times 2$					$\times 4$				
	PSNR \uparrow	SSIM \uparrow	LPIPS \downarrow	DISTS \downarrow	FID \downarrow	PSNR \uparrow	SSIM \uparrow	LPIPS \downarrow	DISTS \downarrow	FID \downarrow
MIRNet-v2 [69] → SwinIR [35]	21.74	0.8446	0.4451	0.2498	156.31	21.44	0.8619	0.5050	0.2600	160.33
USRNet [72]	18.09	0.8243	0.4291	0.3029	181.18	18.00	0.8412	0.4333	0.3221	190.65
RealSR [25]	-	-	-	-	-	18.56	0.7961	0.4221	0.2476	153.27
Real-ESRGAN [59]	21.72	0.8641	0.2592	0.1735	108.43	19.94	0.8530	0.3224	0.2086	138.97
SwinIR [35]	21.25	0.8522	0.3946	0.2344	136.95	20.70	0.8609	0.4858	0.2554	147.47
Ours	24.24	0.8658	0.3493	0.1764	107.09	21.62	0.8640	0.4326	0.1896	125.13



Figure 5. Qualitative visual comparisons for $\times 2$ SR (-3 EV, ISO 3200) on our SRRRIE dataset. The compared methods restore noticeable color distortions and artifacts while our method generates photo-realistic results with nature face structures.

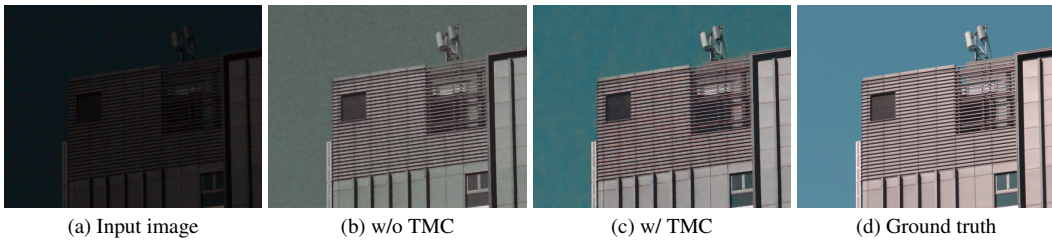


Figure 6. Qualitative visual evaluations on the proposed TMC (Eq. (9)). The generated image with TMC exhibits more realistic textures and truthful colors. In contrast, the resulting image without TMC suffers from color distortion and contains more remain noises in the sky.

7. Analysis and Discussions

7.1. Effectiveness of the time-melding condition

Our proposed time-melding condition (TMC) fuses valuable information across relevant time points. The recursively strategy facilitates preserving detail and visual fidelity from multiple frames for the progressively generation

process in Eq.(10). To demonstrate its effectiveness, we disable Eq. (9) in the proposed method and retrain with the same settings for fair comparisons. Figure 6 (c) shows the result using TMC, where the structural details and colors are restored well. In contrast, the result without TMC contains more remain noises and color distortion as shown in Figure

Table 3. Effectiveness of the proposed TMC (Eq. (9)) on the validation set. The proposed TMC could effectively improve the reverse generation process to obtain better image quality.

Method	PSNR \uparrow	SSIM \uparrow	LPIPS \downarrow	DISTS \downarrow
w/o TMC	20.83	0.8644	0.4417	0.2794
w/ TMC	22.64	0.8720	0.3671	0.2506

Table 4. Quantitative evaluations of the methods trained on real Raw sensor data and 8-bit sRGB data of our SRRRIE dataset.

Scale	Method	PSNR \uparrow	SSIM \uparrow	LPIPS \downarrow	DISTS \downarrow
$\times 2$	Ours-sRGB	23.98	0.8457	0.4572	0.2366
	Ours-Raw	24.50	0.8654	0.3652	0.1910
$\times 4$	Ours-sRGB	22.64	0.8570	0.5470	0.2478
	Ours-Raw	22.80	0.8690	0.4750	0.2210

6 (b). The quantitative comparisons in Table 3 demonstrates that using TMC achieves better restoration results in terms of PSNR, SSIM, LPIPS and DISTS metrics on the validation set of our SRRRIE dataset. Our conditional DPM-based method benefits from the time-melding condition, thus further improves the consistency and robustness of the reverse generation process to generate better image quality.

7.2. Effectiveness of the Raw sensor data

We provide both Raw sensor data and sRGB data for our SRRRIE dataset. To demonstrate the effectiveness of the real Raw sensor data, we retrain our diffusion model and disable π in Eq. (8). Figure 7 shows the qualitative visual results, where our method trained on Raw images achieves clearer and sharper face structures. The quantitative results summarized in Table 4 demonstrate that real Raw sensor data could consistently improve the restoration performances against the sRGB data in terms of both reconstruction and perceptual metrics. Raw sensor data contains valuable information that is necessary for accurate restoration and enhancement, making it beneficial for image restoration. In contrast, the compression process used for low-bit sRGB images causes the loss of essential structures and details, leading to more ill-posed problems. Therefore, these experiments indicate that Raw sensor data is a better option for super-resolving real-world image illumination enhancement tasks as it maintains the lossless information required for restoration and enhancement.

7.3. Cross-dataset generalization

Our SRRRIE dataset is captured using a Sony A7 IV camera, with exposure levels ranging from -6 EV to 0 EV and ISO levels ranging from 50 to 12800. To assess the generalizability across different sensors and datasets, we employ cross-validation by training the model on one dataset and testing it on the other dataset. The RELISUR dataset is captured using a Canon camera, with exposure levels ranging from -5 EV to -2.5 EV and ISO levels ranging from 100 to 400. In Table 5, we summarize the results of the model trained on RELISUR and SRRRIE datasets, respectively. The results show that the model trained on SRRRIE dataset still performs well on RELISUR dataset, whereas

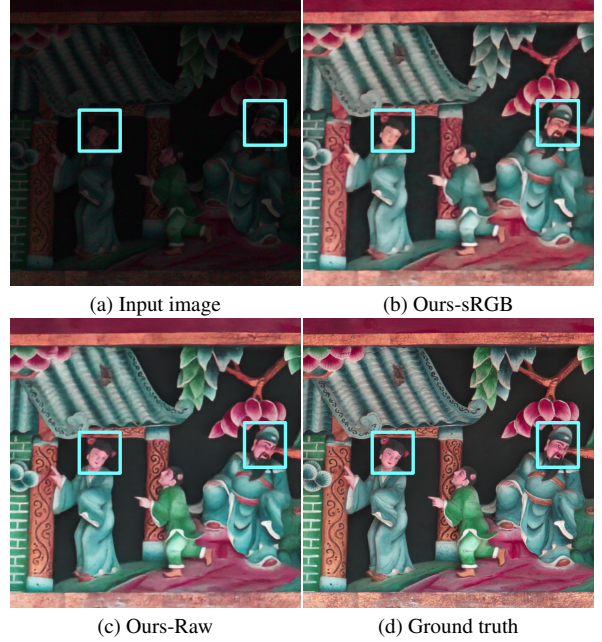


Figure 7. The method trained on real Raw sensor data could restore more truthful and clear face details compared to the method trained on sRGB images.

Table 5. Cross-dataset generalization test in terms of PSNR/SSIM. We train our network on one dataset then test on the other dataset.

Method	Trained	Tested	
		RELISUR (Canon)	SRRRIE (Sony)
Ours-sRGB	RELISUR	24.64/0.8167	19.26/0.5551
	SRRRIE	20.65/0.7601	23.98/0.8457

the model trained on RELISUR dataset performs less effectively on SRRRIE dataset. The SRRRIE dataset contains real-world degradation processes in low-light conditions with complicated noises, making it more challenging.

8. Conclusions

In this paper, we have addressed the need for a high-quality Raw image dataset for super-resolving real-world illumination enhancement tasks. Towards this goal, we collect 4800 paired low-high quality images with a wide range of under exposure levels from -6 EV to 0 EV and ISO levels from 50 to 12800. We conduct comprehensive benchmark experiments for existing methods on the proposed SRRRIE dataset with various reconstruction and perceptual metrics. As existing methods perform less effectively in real-world restoration problems with complicated noises, we develop a conditional DPM-based method to progressively generate truthful structural details from real Raw sensor data. Our proposed method achieves promising results in both quantitative and qualitative experiments compared to state-of-the-art methods. We hope that our SRRRIE dataset as well as the proposed conditional diffusion process model will advance super-resolving real-world illumination enhancement tasks.

References

- [1] Andreas Aakerberg, Kamal Nasrollahi, and Thomas B Moeslund. Rellisur: A real low-light image super-resolution dataset. In *NeurIPS Datasets and Benchmarks*, 2021. 2, 3, 4, 5, 17, 18
- [2] Abdelrahman Abdelhamed, Stephen Lin, and Michael S Brown. A high-quality denoising dataset for smartphone cameras. In *CVPR*, pages 1692–1700, 2018. 3, 4
- [3] Eirikur Agustsson and Radu Timofte. Ntire 2017 challenge on single image super-resolution: Dataset and study. In *CVPR workshops*, pages 126–135, 2017. 2
- [4] Jimmy Lei Ba, Jamie Ryan Kiros, and Geoffrey E Hinton. Layer normalization. *arXiv preprint*, 2016. 12
- [5] Arpit Bansal, Eitan Borgnia, Hong-Min Chu, Jie S Li, Hamid Kazemi, Furong Huang, Micah Goldblum, Jonas Geiping, and Tom Goldstein. Cold diffusion: Inverting arbitrary image transforms without noise. *arXiv preprint*, 2022. 3, 6, 12
- [6] Marco Bevilacqua, Aline Roumy, Christine Guillemot, and Marie Line Alberi-Morel. Low-complexity single-image super-resolution based on nonnegative neighbor embedding. 2012. 2
- [7] Jianrui Cai, Shuhang Gu, and Lei Zhang. Learning a deep single image contrast enhancer from multi-exposure images. *IEEE TIP*, 27(4):2049–2062, 2018. 2
- [8] Jianrui Cai, Hui Zeng, Hongwei Yong, Zisheng Cao, and Lei Zhang. Toward real-world single image super-resolution: A new benchmark and a new model. In *ICCV*, pages 3086–3095, 2019. 2, 3
- [9] Chen Chen, Qifeng Chen, Jia Xu, and Vladlen Koltun. Learning to see in the dark. In *CVPR*, pages 3291–3300, 2018. 2, 3, 5
- [10] Chang Chen, Zhiwei Xiong, Xinmei Tian, Zheng-Jun Zha, and Feng Wu. Camera lens super-resolution. In *CVPR*, pages 1652–1660, 2019. 2, 3
- [11] Hanting Chen, Yunhe Wang, Tianyu Guo, Chang Xu, Yiping Deng, Zhenhua Liu, Siwei Ma, Chunjing Xu, Chao Xu, and Wen Gao. Pre-trained image processing transformer. In *CVPR*, pages 12299–12310, 2021. 3
- [12] Hyungjin Chung, Byeongsu Sim, and Jong Chul Ye. Come-closer-diffuse-faster: Accelerating conditional diffusion models for inverse problems through stochastic contraction. In *CVPR*, pages 12413–12422, 2022. 3
- [13] Dinu Coltuc, Philippe Bolon, and J-M Chassery. Exact histogram specification. *IEEE TIP*, 15(5):1143–1152, 2006. 2
- [14] Florinel-Alin Croitoru, Vlad Hondru, Radu Tudor Ionescu, and Mubarak Shah. Diffusion models in vision: A survey. *arXiv preprint arXiv:2209.04747*, 2022. 3
- [15] Zihang Dai, Zhilin Yang, Yiming Yang, Jaime Carbonell, Quoc V Le, and Ruslan Salakhutdinov. Transformer-xl: Attentive language models beyond a fixed-length context. *arXiv preprint*, 2019. 12
- [16] Prafulla Dhariwal and Alexander Nichol. Diffusion models beat gans on image synthesis. *NeurIPS*, 34:8780–8794, 2021. 3, 5, 12
- [17] Keyan Ding, Kede Ma, Shiqi Wang, and Eero P. Simoncelli. Image quality assessment: Unifying structure and texture similarity. *CoRR*, abs/2004.07728, 2020. 6, 7
- [18] Vincent Dumoulin and Francesco Visin. A guide to convolution arithmetic for deep learning. *arXiv preprint*, 2016. 12
- [19] Jinsheng Fang, Hanjiang Lin, Xinyu Chen, and Kun Zeng. A hybrid network of cnn and transformer for lightweight image super-resolution. In *CVPR Workshops*, pages 1103–1112, June 2022. 3
- [20] Xiaojie Guo, Yu Li, and Haibin Ling. LIME: Low-light image enhancement via illumination map estimation. *IEEE TIP*, 26(2):982–993, 2016. 2
- [21] Kaiming He, Xiangyu Zhang, Shaoqing Ren, and Jian Sun. Deep residual learning for image recognition. In *CVPR*, pages 770–778, 2016. 12
- [22] Dan Hendrycks and Kevin Gimpel. Gaussian error linear units (gelus). *arXiv preprint*, 2016. 12
- [23] Jonathan Ho, Ajay Jain, and Pieter Abbeel. Denoising diffusion probabilistic models. *NeurIPS*, 33:6840–6851, 2020. 3, 5, 12
- [24] Haidi Ibrahim and Nicholas Sia Pik Kong. Brightness preserving dynamic histogram equalization for image contrast enhancement. *IEEE Transactions on Consumer Electronics*, 53(4):1752–1758, 2007. 2
- [25] Xiaozhong Ji, Yun Cao, Ying Tai, Chengjie Wang, Jilin Li, and Feiyue Huang. Real-world super-resolution via kernel estimation and noise injection. In *CVPR Workshops*, June 2020. 7, 19
- [26] Yifan Jiang, Xinyu Gong, Ding Liu, Yu Cheng, Chen Fang, Xiaohui Shen, Jianchao Yang, Pan Zhou, and Zhangyang Wang. EnlightenGAN: Deep light enhancement without paired supervision. *IEEE TIP*, PP:1–1, 01 2021. 2
- [27] Bahjat Kwar, Michael Elad, Stefano Ermon, and Jiaming Song. Denoising diffusion restoration models. *arXiv preprint arXiv:2201.11793*, 2022. 3
- [28] Jiwon Kim, Jung Kwon Lee, and Kyoung Mu Lee. Accurate image super-resolution using very deep convolutional networks. In *CVPR*, pages 1646–1654, 2016. 2
- [29] Diederik P Kingma and Jimmy Ba. Adam: A method for stochastic optimization. *arXiv preprint arXiv:1412.6980*, 2014. 6
- [30] Christian Ledig, Lucas Theis, Ferenc Huszár, Jose Caballero, Andrew Cunningham, Alejandro Acosta, Andrew Aitken, Alykhan Tejani, Johannes Totz, Zehan Wang, et al. Photo-realistic single image super-resolution using a generative adversarial network. In *CVPR*, pages 4681–4690, 2017. 2
- [31] Chulwoo Lee, Chul Lee, and Chang-Su Kim. Contrast enhancement based on layered difference representation of 2D histograms. *IEEE TIP*, 22(12):5372–5384, 2013. 2
- [32] Chongyi Li, Chunle Guo, and Chen Change Loy. Learning to enhance low-light image via zero-reference deep curve estimation. *IEEE TPAMI*, 44(8):4225–4238, 2022. 1, 2
- [33] Haoying Li, Yifan Yang, Meng Chang, Shiqi Chen, Huajun Feng, Zhihai Xu, Qi Li, and Yueting Chen. Srdiff: Single image super-resolution with diffusion probabilistic models. *Neurocomputing*, 479:47–59, 2022. 3
- [34] Mading Li, Jiaying Liu, Wenhan Yang, Xiaoyan Sun, and Zongming Guo. Structure-revealing low-light image enhancement via robust retinex model. *IEEE TIP*, 27(6):2828–2841, 2018. 2

- [35] Jingyun Liang, Jiezhong Cao, Guolei Sun, Kai Zhang, Luc Van Gool, and Radu Timofte. Swinir: Image restoration using swin transformer. In *ICCV Workshops*, pages 1833–1844, 2021. 1, 2, 3, 6, 7, 13, 14, 19
- [36] Bee Lim, Sanghyun Son, Heewon Kim, Seungjun Nah, and Kyoung Mu Lee. Enhanced deep residual networks for single image super-resolution. In *CVPR Workshops*, pages 136–144, 2017. 2
- [37] Risheng Liu, Long Ma, Jiaao Zhang, Xin Fan, and Zhongxuan Luo. Retinex-inspired unrolling with cooperative prior architecture search for low-light image enhancement. In *CVPR*, pages 10561–10570, 2021. 1, 2
- [38] Zhuang Liu, Hanzi Mao, Chao-Yuan Wu, Christoph Feichtenhofer, Trevor Darrell, and Saining Xie. A convnet for the 2020s. In *CVPR*, pages 11976–11986, 2022. 12
- [39] Ilya Loshchilov and Frank Hutter. Sgdr: Stochastic gradient descent with warm restarts. *arXiv preprint*, 2016. 6
- [40] David G Lowe. Distinctive image features from scale-invariant keypoints. *IJCV*, 60:91–110, 2004. 4
- [41] Andreas Lugmayr, Martin Danelljan, Luc Van Gool, and Radu Timofte. Srflo: Learning the super-resolution space with normalizing flow. In *ECCV*, pages 715–732. Springer, 2020. 2
- [42] Kede Ma, Kai Zeng, and Zhou Wang. Perceptual quality assessment for multi-exposure image fusion. *IEEE TIP*, 24(11):3345–3356, 2015. 2
- [43] David Martin, Charless Fowlkes, Doron Tal, and Jitendra Malik. A database of human segmented natural images and its application to evaluating segmentation algorithms and measuring ecological statistics. In *ICCV*, volume 2, pages 416–423, 2001. 2
- [44] Ozan Özdenizci and Robert Legenstein. Restoring vision in adverse weather conditions with patch-based denoising diffusion models. *IEEE TPAMI*, pages 1–12, 2023. 3, 5
- [45] Xutong Ren, Wenhan Yang, Wen-Huang Cheng, and Jiaying Liu. LR3M: Robust low-light enhancement via low-rank regularized retinex model. *IEEE TIP*, 29:5862–5876, 2020. 2
- [46] Robin Rombach, Andreas Blattmann, Dominik Lorenz, Patrick Esser, and Björn Ommer. High-resolution image synthesis with latent diffusion models. In *CVPR*, pages 10684–10695, 2022. 3, 5, 12
- [47] Olaf Ronneberger, Philipp Fischer, and Thomas Brox. U-net: Convolutional networks for biomedical image segmentation. In *MICCAI*, pages 234–241, 2015. 5
- [48] Chitwan Saharia, William Chan, Saurabh Saxena, Lala Li, Jay Whang, Emily Denton, Seyed Kamyar Seyed Ghasemipour, Burcu Karagol Ayan, S Sara Mahdavi, Rapha Gontijo Lopes, et al. Photorealistic text-to-image diffusion models with deep language understanding. *arXiv preprint*, 2022. 5
- [49] Chitwan Saharia, Jonathan Ho, William Chan, Tim Salimans, David J Fleet, and Mohammad Norouzi. Image super-resolution via iterative refinement. *IEEE TPAMI*, 2022. 3
- [50] Maximilian Seitzer. pytorch-fid: FID Score for PyTorch, 2020. 6, 7
- [51] Jascha Sohl-Dickstein, Eric Weiss, Niru Maheswaranathan, and Surya Ganguli. Deep unsupervised learning using nonequilibrium thermodynamics. In *ICML*, pages 2256–2265, 2015. 3, 5
- [52] Jiaming Song, Chenlin Meng, and Stefano Ermon. Denoising diffusion implicit models. In *ICLR*, 2021. 5, 6, 12
- [53] Yang Song and Stefano Ermon. Generative modeling by estimating gradients of the data distribution. *NeurIPS*, 32, 2019. 3
- [54] Yang Song, Jascha Sohl-Dickstein, Diederik P Kingma, Abhishek Kumar, Stefano Ermon, and Ben Poole. Score-based generative modeling through stochastic differential equations. *arXiv preprint arXiv:2011.13456*, 2020. 3
- [55] J Alex Stark. Adaptive image contrast enhancement using generalizations of histogram equalization. *IEEE TIP*, 9(5):889–896, 2000. 2
- [56] Ying Tai, Jian Yang, and Xiaoming Liu. Image super-resolution via deep recursive residual network. In *CVPR*, pages 3147–3155, 2017. 2
- [57] Radu Timofte, Vincent De Smet, and Luc Van Gool. A+: Adjusted anchored neighborhood regression for fast super-resolution. In *ACCV*, pages 111–126, 2014. 2
- [58] Ashish Vaswani, Noam Shazeer, Niki Parmar, Jakob Uszkoreit, Llion Jones, Aidan N Gomez, Łukasz Kaiser, and Illia Polosukhin. Attention is all you need. *NeurIPS*, 30, 2017. 12
- [59] Xintao Wang, Liangbin Xie, Chao Dong, and Ying Shan. Real-esrgan: Training real-world blind super-resolution with pure synthetic data. In *ICCV Workshops*. 1, 2, 6, 7, 12, 19
- [60] Xintao Wang, Liangbin Xie, Chao Dong, and Ying Shan. Real-esrgan: Training real-world blind super-resolution with pure synthetic data. In *ICCV*, pages 1905–1914, 2021. 2
- [61] Xintao Wang, Ke Yu, Shixiang Wu, Jinjin Gu, Yihao Liu, Chao Dong, Yu Qiao, and Chen Change Loy. Esrgan: Enhanced super-resolution generative adversarial networks. In *ECCV Workshops*, 2018. 2
- [62] Yufei Wang, Renjie Wan, Wenhan Yang, Haoliang Li, Lap-Pui Chau, and Alex Kot. Low-light image enhancement with normalizing flow. In *AAAI*, volume 36, pages 2604–2612, 2022. 1, 2
- [63] Chen Wei, Wenjing Wang, Wenhan Yang, and Jiaying Liu. Deep retinex decomposition for low-light enhancement. In *BMVC*, 2018. 2, 3
- [64] Pengxu Wei, Ziwei Xie, Hannan Lu, Zongyuan Zhan, Qixiang Ye, Wangmeng Zuo, and Liang Lin. Component divide-and-conquer for real-world image super-resolution. In *ECCV*, pages 101–117, 2020. 2, 3
- [65] Jay Whang, Mauricio Delbracio, Hossein Talebi, Chitwan Saharia, Alexandros G Dimakis, and Peyman Milanfar. Deblurring via stochastic refinement. In *CVPR*, pages 16293–16303, 2022. 3
- [66] Jianchao Yang, John Wright, Thomas S Huang, and Yi Ma. Image super-resolution via sparse representation. *IEEE TIP*, 19(11):2861–2873, 2010. 2
- [67] Ling Yang, Zhilong Zhang, Yang Song, Shenda Hong, Runsheng Xu, Yue Zhao, Yingxia Shao, Wentao Zhang, Bin Cui, and Ming-Hsuan Yang. Diffusion models: A comprehensive survey of methods and applications. *arXiv preprint arXiv:2209.00796*, 2022. 3

- [68] Wenhan Yang, Shiqi Wang, Yuming Fang, Yue Wang, and Jiaying Liu. From fidelity to perceptual quality: A semi-supervised approach for low-light image enhancement. In *CVPR*, June 2020. [2](#)
- [69] Syed Waqas Zamir, Aditya Arora, Salman Khan, Munawar Hayat, Fahad Shahbaz Khan, Ming-Hsuan Yang, and Ling Shao. Learning enriched features for fast image restoration and enhancement. *IEEE TPAMI*, 2022. [1](#), [2](#), [6](#), [7](#), [13](#), [14](#), [19](#)
- [70] Roman Zeyde, Michael Elad, and Matan Protter. On single image scale-up using sparse-representations. In *ICCS*, pages 711–730, 2010. [2](#)
- [71] Kai Zhang, Jingyun Liang, Luc Van Gool, and Radu Timofte. Designing a practical degradation model for deep blind image super-resolution. In *ICCV*, pages 4791–4800, 2021. [2](#)
- [72] Kai Zhang, Luc Van Gool, and Radu Timofte. Deep unfolding network for image super-resolution. In *CVPR*, pages 3217–3226, 2020. [1](#), [2](#), [6](#), [7](#), [19](#)
- [73] Richard Zhang, Phillip Isola, Alexei A Efros, Eli Shechtman, and Oliver Wang. The unreasonable effectiveness of deep features as a perceptual metric. In *CVPR*, 2018. [6](#), [7](#)
- [74] Xuaner Zhang, Qifeng Chen, Ren Ng, and Vladlen Koltun. Zoom to learn, learn to zoom. In *CVPR*, pages 3762–3770, 2019. [2](#), [3](#)
- [75] Yulun Zhang, Yapeng Tian, Yu Kong, Bineng Zhong, and Yun Fu. Residual dense network for image super-resolution. In *CVPR*, pages 2472–2481, 2018. [2](#)
- [76] Yonghua Zhang, Jiawan Zhang, and Xiaojie Guo. Kindling the darkness: A practical low-light image enhancer. In *ACM Multimedia*, pages 1632–1640, 2019. [2](#)

Appendix

This supplementary document provides a more comprehensive analysis of our proposed dataset and method. We present the training approach in Section A and the detailed network architecture in Section B. In Section C, we analyze the limitations of our proposed method. While in Section D, we analyze cascaded methods and joint methods. We also provide more statistical analysis of our proposed SR-RIE dataset in Section E. Finally, we demonstrate more qualitative visual results on various scenes and compare our method with state-of-the-art algorithms in Section F. The results shown in this supplementary material are best viewed on a high-resolution display.

A. Details of the Training Approach

The variational inference objective [23, 16, 52] is employed to train the Gaussian denoisers utilized in Eq. (4) of the manuscript within diffusion probabilistic models:

$$L_\theta = \mathbb{E}_{q_\sigma} \left[\underbrace{D_{KL}(q_\sigma(x_T | x_0) || p_\theta(x_T))}_{L_\theta^T} - \underbrace{\log p_\theta(x_0 | x_1)}_{L_\theta^0} + \sum_{t=2}^T \underbrace{D_{KL}(q_\sigma(x_{t-1} | x_t, x_0) || p_\theta^{(t)}(x_{t-1} | x_t))}_{L_\theta^{t-1}} \right], \quad (11)$$

where L_θ^{t-1} could be simplified using the alternative reparameterization that replace μ_θ with ϵ_θ and employs a re-weighted optimization strategy [23, 52]:

$$L_\theta^{(t-1)} = \mathbb{E}_{x_0, \epsilon_t, t} [\|\epsilon_t - \epsilon_\theta(\sqrt{\alpha_t}x_0 + \sqrt{1 - \alpha_t}\epsilon_t, t)\|^2], \quad (12)$$

where $\epsilon_t \sim \mathcal{N}(\mathbf{0}, \mathbf{I})$. We introduce two novel conditions $\pi(\tilde{x})$ and $\bar{\mu}_\theta^{(t)}$ for the reverse generation process described in Eq. (10) of the manuscript. Using these conditions, we develop new Gaussian denoisers, denoted as $\hat{\mu}_\theta(x_t, \pi(\tilde{x}), \bar{\mu}_\theta^{(t+1)}, t)$, to estimate the value of x_{t-1} . To update Eq. (13), we apply a reparameterization technique similar to that used for $\hat{\epsilon}_\theta(x_t, \pi(\tilde{x}), \bar{\mu}_\theta^{(t+1)})$:

$$L_\theta^{(t-1)} = \mathbb{E}_{x_0, \pi(\tilde{x}), \epsilon_t, t} [\|\epsilon_t - \hat{\epsilon}_\theta(\sqrt{\alpha_t}x_0 + \sqrt{1 - \alpha_t}\epsilon_t, \pi(\tilde{x}), \bar{\mu}_\theta^{(t+1)}, t)\|^2], \quad (13)$$

In Section 3.1 of the manuscript, we provide 400 paired low-high quality images for super-resolving real-world image illumination enhancement tasks. Each sequence consists of 9 low-light images, serving as low-quality images, and 3 high-resolution images, serving as the ground truth high-quality images. We use the 9 low-light images to represent the condition $\pi(\tilde{x})$, while the 3 high-resolution images defined in Eq. (2) represent x_0 . We jointly train the denoisers $\{\hat{\epsilon}_\theta(\sqrt{\alpha_t}x_0 + \sqrt{1 - \alpha_t}\epsilon_t, \pi(\tilde{x}), \bar{\mu}_\theta^{(t+1)}, t)\}_{t=0}^T$ with modern deep learning techniques.

B. Network Architecture

We describe the detailed network architecture for $\{\hat{\epsilon}_\theta(\sqrt{\alpha_t}x_0 + \sqrt{1 - \alpha_t}\epsilon_t, \pi(\tilde{x}), \bar{\mu}_\theta^{(t+1)}, t)\}_{t=0}^T$. The deep networks share the same network architecture weights parameters across different sampling t during training and test. As summarized in Table 6, the proposed denoiser is based on a U-Net architecture motivated by prior works [23, 52, 5]. This network incorporates downsampling and upsampling paths using ConvNext blocks [38] and residual blocks [21], while employing a sinusoidal positional embedding operation [15] for time embedding. As summarized in Table 7, the ConvNext block architecture includes a time multi-layer perceptron (MLP) and a convolutional network. And the ConvNext block architecture features the Gaussian error linear unit (GELU) activation function [22] and layer normalization (LayerNorm) [4]. As summarized in Table 8, the residual block architecture utilizes pre-layer normalization [4] and linear attention [58] components. The downsampling path uses convolutional layers, while the upsampling path employs transposed convolutional layers [18]. The network processing Raw images before the diffusion model shares a similar architecture to the denoising U-Net, except for three variations: 4 initial input channels, 3 final output channels, and channels 16 times smaller than the denoising U-Net, without incorporating time embedding.

C. Limitation Analysis on the Proposed Method

Our proposed conditional diffusion probabilistic model employs default network architectures used in state-of-the-art diffusion model works [52, 5]. However, its main limitation is the longer inference time compared to one-step forward deep learning-based methods. For instance, DDPM [23] requires 1000 rounds of computationally expensive Langevin dynamics sampling. To address the slow speed issue, DDIM [52] accelerates sampling with effective deterministic implicit sampling, while Stable Diffusion [46] trains a more efficient diffusion model by embedding data into a latent space. Although these methods perform well, our proposed model takes one minute to restore a 512×512 image with 50 sample steps on a single NVIDIA A6000 GPU, whereas Real-ESRGAN [59] only takes 0.7 seconds. Thus, there is still a need for further research to develop more efficient algorithms for diffusion probabilistic models that can be applied to a wider range of practical problems.

D. Analysis on Cascaded Methods and Joint Methods

As analyzed in Section 1 of the manuscript, we could directly use existing single image illumination enhancement methods and super-resolution methods separately in a cas-

Table 6. Proposed denosing U-Net architecture.

Layer	Input Channels	Output Channels	Kernel Size	Activation
Time Embedding Block				
SinusoidalPosEmb	-	64	-	-
MLP	64, 256	256, 64	-	GELU
Downsampling Blocks				
ConvNextBlock \times 2	9, 64	64, 64	1, 3, 7	GELU
ResidualBlock	64	64	1	-
Conv	64	64	4	-
ConvNextBlock \times 2	64, 128	128, 128	1, 3, 7	GELU
ResidualBlock	128	128	1	-
Conv	128	128	4	-
ConvNextBlock \times 2	128, 256	256, 256	1, 3, 7	GELU
ResidualBlock	256	256	1	-
Conv	256	256	4	-
ConvNextBlock \times 2	256, 512	512, 512	1, 3, 7	GELU
ResidualBlock	512	512	1	-
Middle Block				
ConvNextBlock	512	512	3, 7	GELU
ResidualBlock	512	512	1	-
ConvNextBlock	512	512	3, 7	GELU
Upsampling Blocks				
ConvNextBlock \times 2	1024, 256	256, 256	1, 3, 7	GELU
ResidualBlock	256	256	1	-
Transposed Conv	256	256	4	-
ConvNextBlock \times 2	512, 128	128, 128	1, 3, 7	GELU
ResidualBlock	128	128	1	-
Transposed Conv	128	128	4	-
ConvNextBlock \times 2	256, 64	64, 64	1, 3, 7	GELU
ResidualBlock	64	64	1	-
Transposed Conv	64	64	4	-
Output Block				
ConvNextBlock	64	64	3, 7	-
Conv	64	3	1	-

caded manner for super-resolving real-world image illumination enhancement tasks. Figure 8 shows the example results. We first use MIRNet-v2 [69] method (Figure 8 (b)) to enhance the input low-light image, then use SwinIR [35] method (Figure 8 (c)) to super-resolve the enhanced output image by a scale of 4. However, the artifacts and color distortions in Figure 8 (b) are further amplified in Figure 8 (c). In contrast, applying SwinIR [35] method directly to super-resolve image illumination enhancement tasks in a joint manner can avoid these problems, as shown in Figure 8 (d). Furthermore, the quantitative results in Table 2 of

the manuscript indicate that the cascaded method MIRNet-v2 [69] \rightarrow SwinIR [35] achieves higher PSNR values compared to using SwinIR [35] in a joint manner, but performs less effectively in terms of other metrics. These experiments demonstrate that cascaded methods do not always outperform joint methods. The intermediate output of the illumination enhancement model in the first stage may suffer from significant information loss or accumulated incorrect predicted information, resulting in a more ill-posed image restoration problem. Consequently, the super-resolution model in the second stage performs less effectively.



Figure 8. Visual comparisons ($\times 4$ SR) on the SRRiIE dataset for cascaded methods and joint methods. The low-quality input images are captured with -2 EV and high ISO levels, resulting in complicated real-world noises. The intermediate output images of the illumination enhancement model in the first stage contain artifacts and color distortions, which are further amplified in the super-resolution model in the second stage, as seen in (b) and (c). In contrast, the joint method generates more natural images, as shown in (d).

Table 7. Proposed ConvNext block architecture. The number of channels denoted by N differs among blocks.

Layer	Channels	Kernel Size
Time MLP		
GELU	-	-
Linear	$N \rightarrow 4 \times N$	-
Conv Net		
Conv	$4 \times N \rightarrow 4 \times N$	7
LayerNorm	-	-
Conv	$4 \times N \rightarrow 8 \times N$	3
GELU	-	-
Conv	$8 \times N \rightarrow 4 \times N$	3
Conv/Identity	$4 \times N \rightarrow N/-$	1/-

Table 8. Proposed residual block architecture. The number of channels denoted by N differs among blocks.

Layer	Channels	Kernel Size
PreNorm	-	-
Linear Attention		
Conv (to_qkv)	$2 \times N \rightarrow 3 \times N$	1
Conv (to_out)	$N \rightarrow 2 \times N$	1
LayerNorm	-	-

E. Statistical Analysis on the Proposed SRRiIE dataset

In Section 3.1 of the manuscript, we present a comprehensive data collection and processing pipeline for the SRRiIE dataset, which includes 400 paired image sequences of outdoor and indoor scenes captured with a Sony A7 IV camera and Tamron 28-200mm zoom lens. To ensure that the dataset is diverse and representative of real-world scenarios, we selectively split the image sequences, based on categories of image contents and camera ISO levels, into

non-overlapping training and test sets of 300 and 100, respectively. The dataset contains various scenes, such as buildings, sculptures, wall paintings, traffic signs, license plates, and furniture. Examples of 30 normal-light scenes from the training and test sets are shown in Figure 9 and 10, respectively. Each image sequence includes nine low-light low-resolution images (Raw/sRGB) captured with exposure levels ranging from -6 EV to -2 EV and ISO levels ranging from 800 to 12800, and three normal-light high-resolution images (sRGB) captured with 0 EV and ISO 50. A sample image sequence is shown in Figure 11. Both Raw sensor data and sRGB data are provided in the SRRiIE dataset, and the images shown in the manuscript and supplemental material are rendered to sRGB for ease of visualization. Note that the original camera resolution is 4672×7008 and we preprocess each image sequence with different center crop sizes.

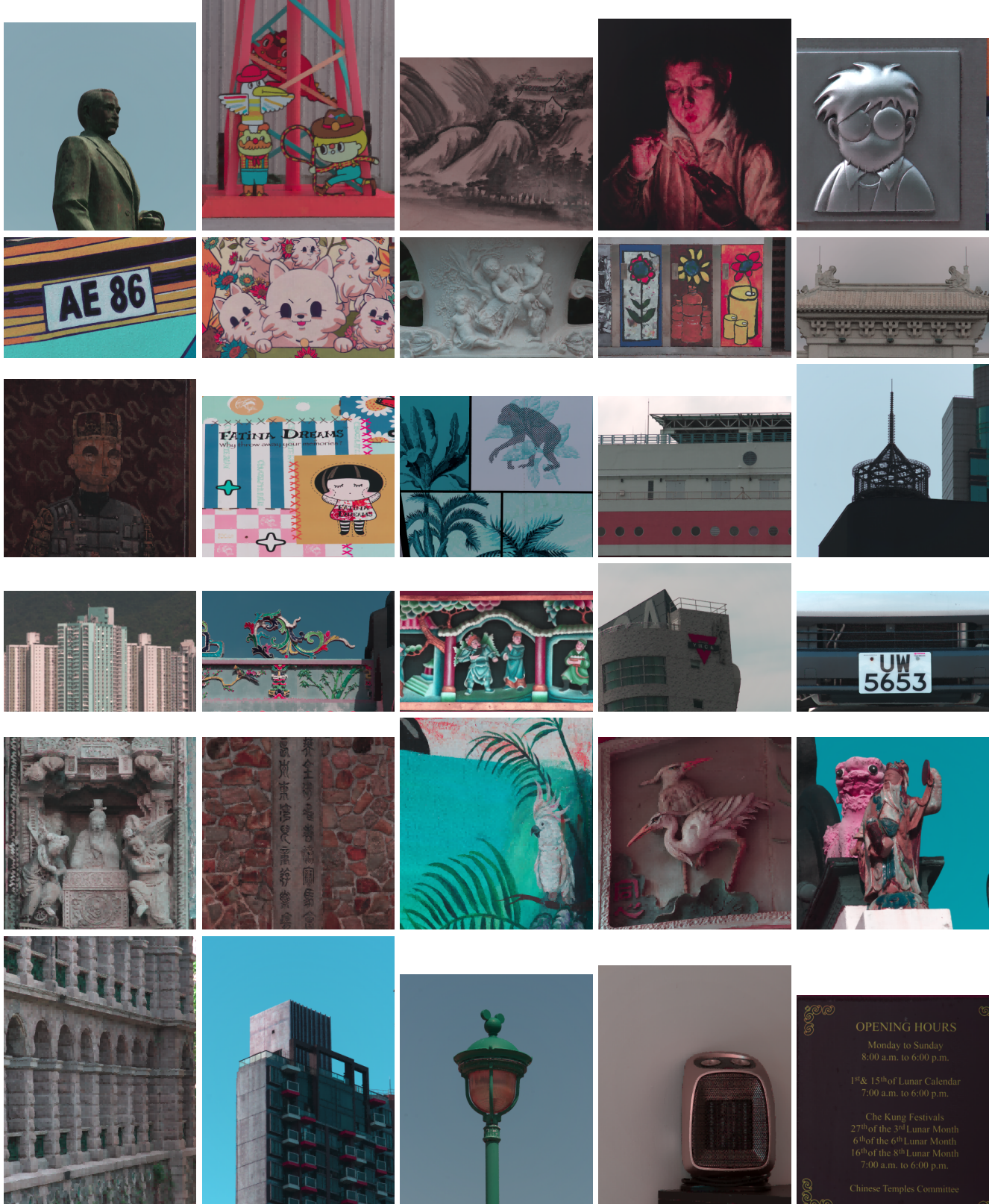


Figure 9. Example normal-light scenes in the train set of our proposed SRRRIE dataset. The train set of our proposed SRRRIE dataset consists of 300 different image sequences captured from 300 non-overlapping outdoor and indoor scenes.

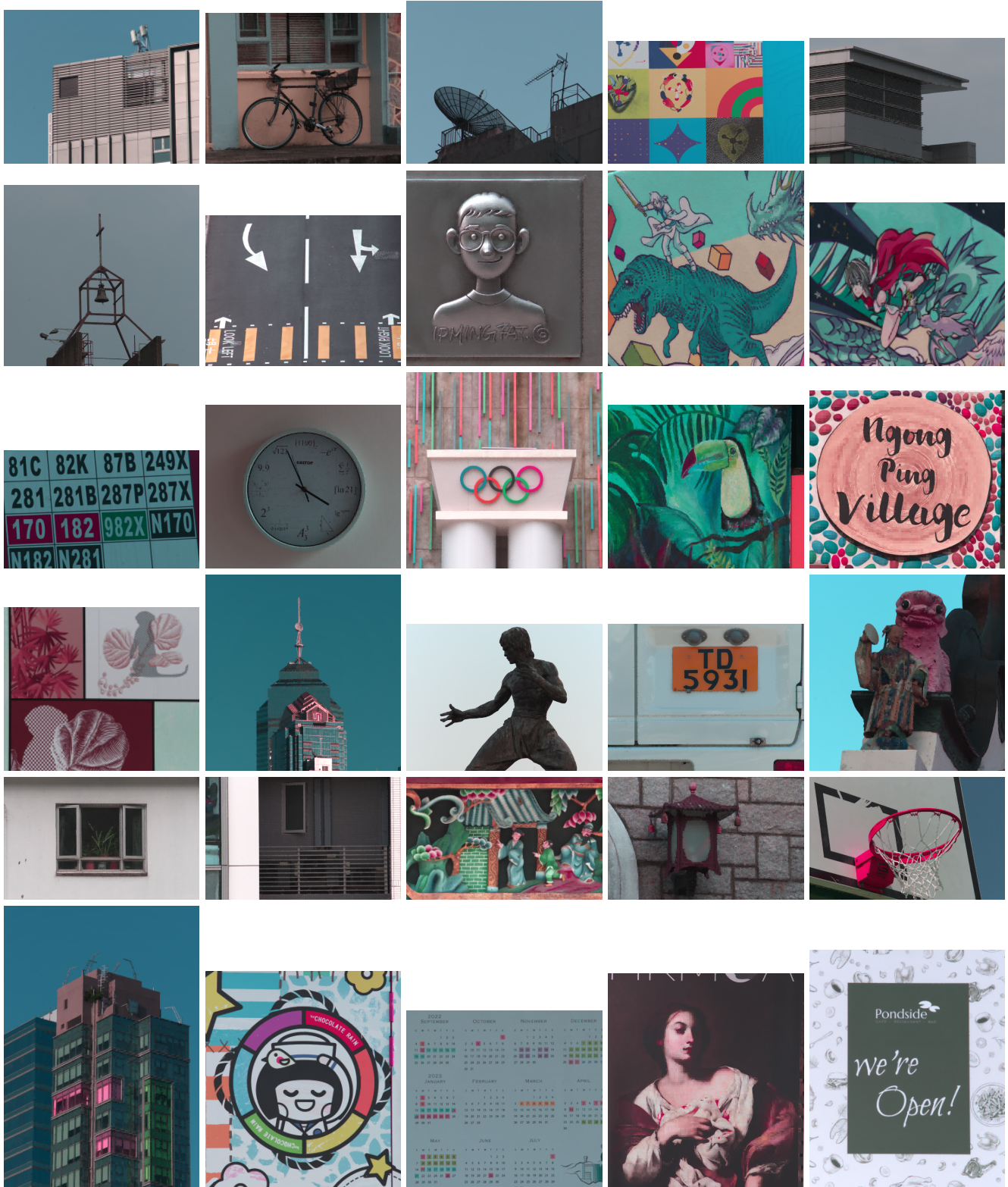


Figure 10. Example normal-light scenes in the test set of our proposed SRRIIE dataset. The test set of our proposed SRRIIE dataset consists of 100 different image sequences captured from 100 non-overlapping outdoor and indoor scenes.

The RELISUR dataset is the most related dataset to our proposed SRRIE dataset [1]. However, it is captured in well-lighted conditions with low ISO levels and does not consider the noise model. Consequently, the low-light images in RELISUR contain less real-world noise. In contrast, our proposed SRRIE dataset is captured with varying exposure levels ranging from -6 EV to 0 EV and ISO levels ranging from 50 to 12800, to model real-world image degradation in low-illumination environments. As a result, the image restoration problems in our dataset are highly ill-posed for existing restoration and enhancement methods. We have illustrated the diverse image gradient distributions of different noisy images in Figure 3 of the manuscript and conducted an ablation study experiment in Section 7.3 of the manuscript to demonstrate cross-dataset generalization using our proposed method. We further summarized the average mean μ and standard deviation value σ of our SRRIE dataset and RELISUR dataset in Table 9 in the supplementary material. Our proposed SRRIE dataset contains a wider range of under-exposure levels and lower signal deviations than the RELISUR dataset. The low contrast and small spread characteristics of our SRRIE dataset make it challenging to learn with existing deep learning-based methods, and these significant differences distinguish our real-world SRRIE dataset from existing datasets such as the RELISUR dataset.

F. More Experimental Results

In Section 6.2 of the manuscript, we compare our proposed method against state-of-the-art algorithms on our proposed SRRIE dataset. We employ multiple reconstruction and perceptual metrics including PSNR, SSIM, LPIPS, DISTS, and FID to benchmark the compared methods. Our comprehensive quantitative and qualitative experimental results demonstrate that our proposed conditional diffusion model-based method outperforms other methods. We present more resulting images on our SRRIE dataset in Figures 12 and 13. We use the publicly available codes of state-of-the-art methods and fine-tune their pre-trained models on our dataset instead of training from scratch to ensure fair comparisons. Our proposed method effectively generates natural results. In contrast, state-of-the-art methods often fail to restore images and generate severe artifacts in the high ill-posed problem of super-resolving real-world image illumination enhancement.

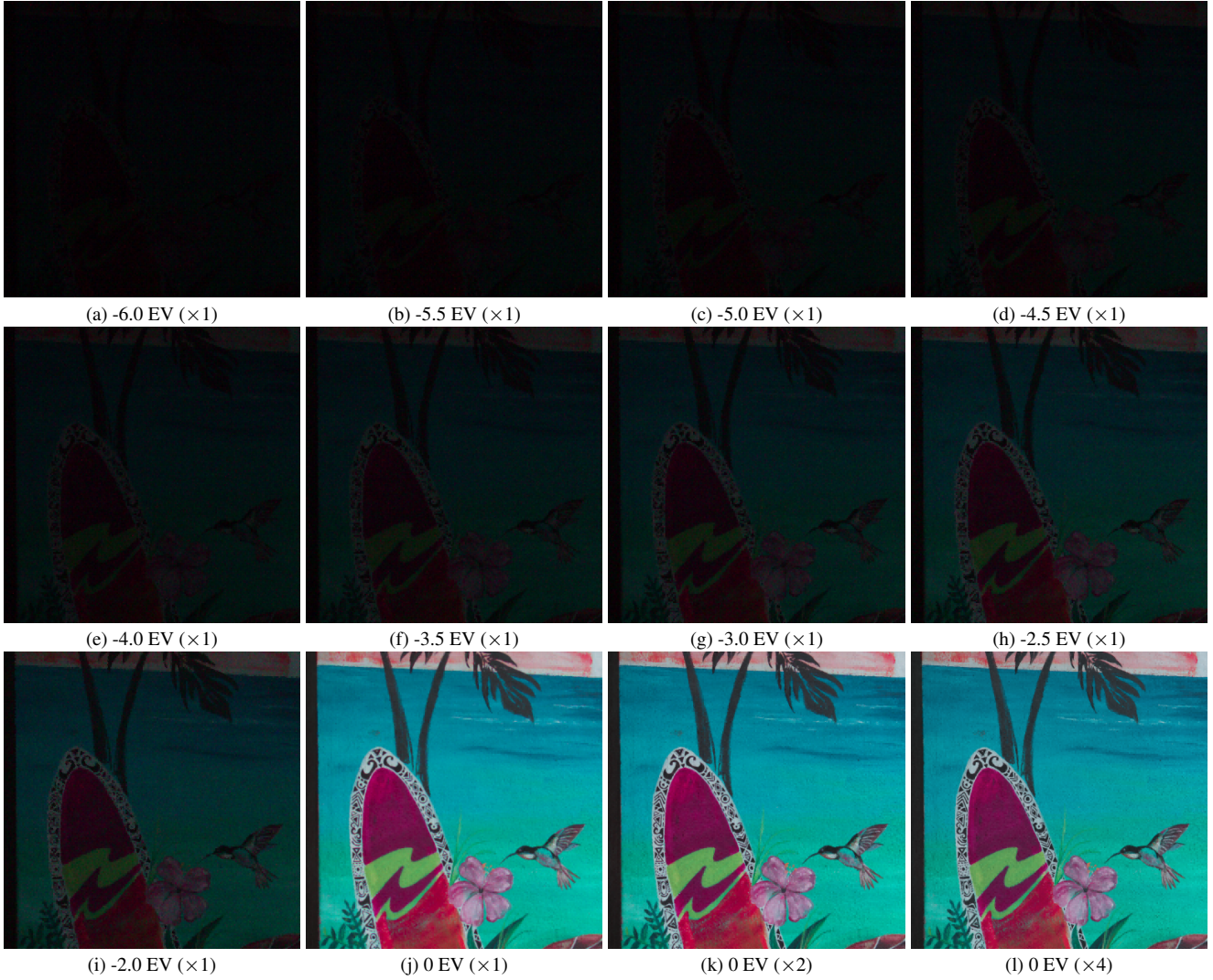


Figure 11. Low-light low-resolution images for each scene are captured with varying under-exposure levels ranging from -6 EV to -2 EV, while normal-light high-resolution images are captured with a fixed 0 EV. The captured low-light images are labeled as (a)-(i), and the normal-light images are labeled as (j)-(l).

Table 9. We compared the mean (μ) and standard deviation (σ) of our SRRRIE dataset to those of the RELLISUR [1] dataset. Our dataset exhibits a wider range of under-exposure levels and lower signal deviations, making it more challenging than the RELLISUR dataset.

Dataset		-2.0 EV	-2.5 EV	-3.0 EV	-3.5 EV	-4.0 EV	-4.5 EV	-5.0 EV	-5.5 EV	-6.0 EV
RELLISUR	μ	-	22.59	17.15	12.20	8.60	6.03	4.29	-	-
	σ	-	16.83	12.76	9.36	6.79	4.91	3.55	-	-
SRRRIE	μ	26.15	20.69	16.38	13.05	10.44	8.45	6.88	5.77	4.98
	σ	10.90	8.68	6.92	5.56	4.50	3.70	3.07	2.67	2.41

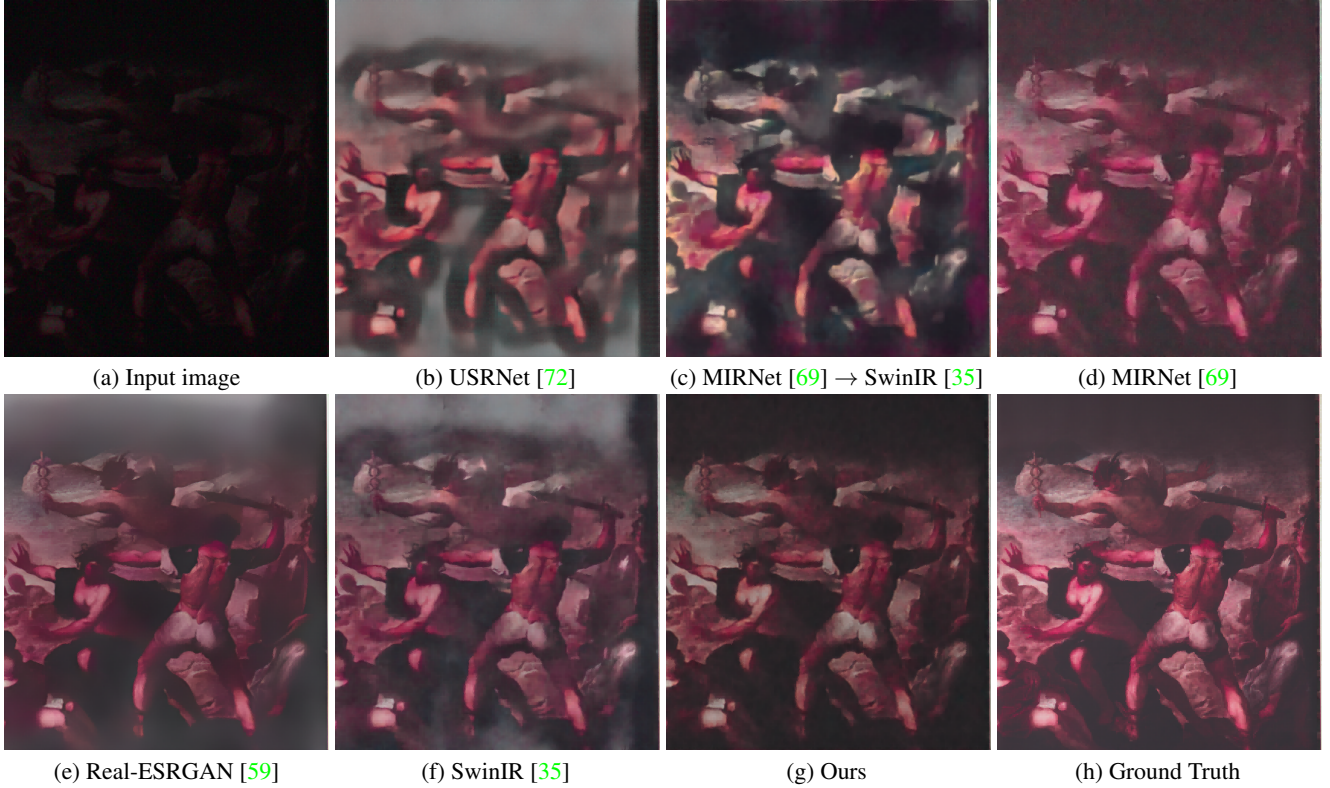


Figure 12. Qualitative visual evaluations ($\times 2$ SR) for the compared methods on the proposed SRRIDE dataset. The low-quality image is captured with the camera settings of -2.5 EV and ISO 4000. While other methods generate severe artifacts, our proposed method restores more natural and visually pleasing results.

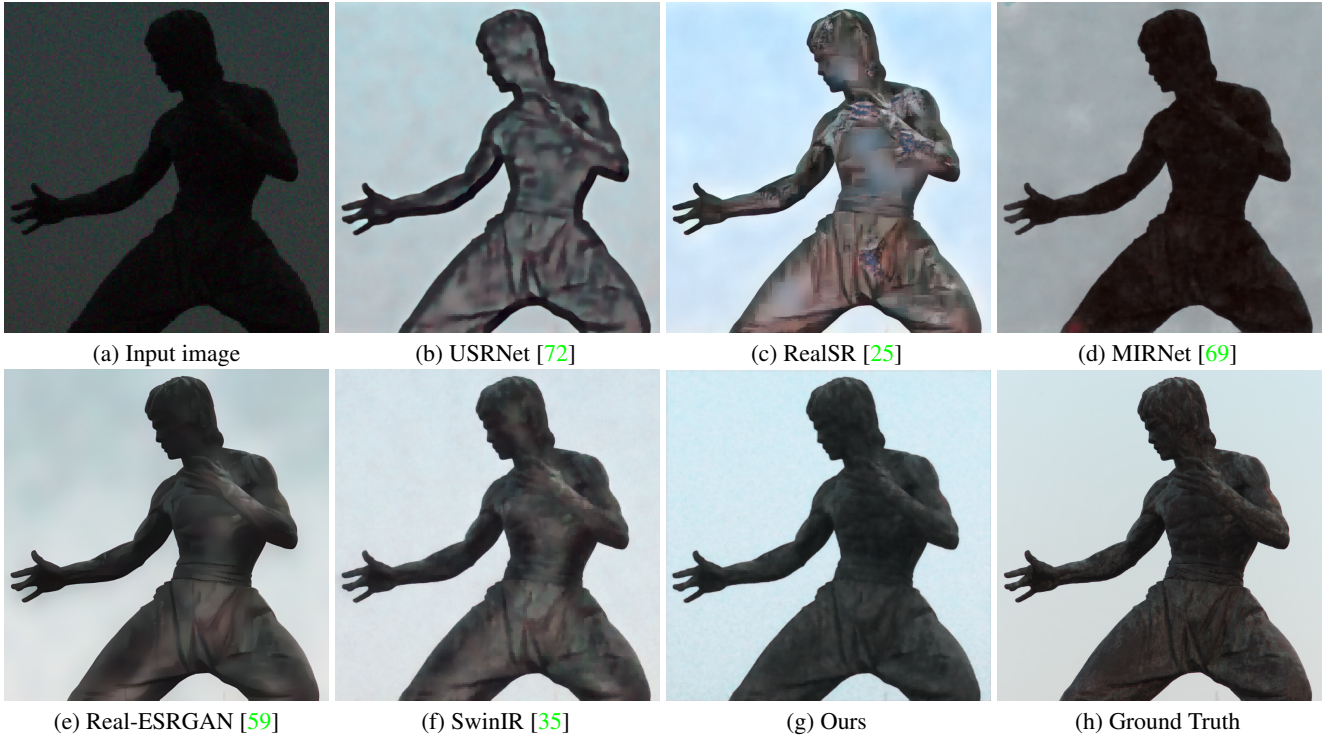


Figure 13. Qualitative visual evaluations ($\times 4$ SR) for the compared methods on the proposed SRRIDE dataset. The low-quality image is captured with the camera settings of -4 EV and ISO 5000. While other methods generated severe artifacts, our proposed method performed favorably as demonstrated by the resulting images.